

# Research Article

doi.org/10.1002/prep.202100214

## Numerical Simulation of Detonation and Brisance Performance of Aluminized HMX Using Density-Adaptive SPH

Jian-Yu Chen,<sup>[a]</sup> Dian-Lei Feng,<sup>[b]</sup> Guang-Yu Wang,<sup>\*[a]</sup> Fei Gao,<sup>[a]</sup> and Chong Peng<sup>[c]</sup>

**Abstract:** The prediction of the brisance performance of the aluminized explosive detonation, which involves complicated multiphase and multiphysics flow, is a difficult problem to tackle. In this paper, the detonation and brisance performance of aluminized HMX explosives is investigated using the density-adaptive smoothed particle hydrodynamics methodology. The ignition and growth model was incorporated in smoothed particle hydrodynamics to calculate the pressure generated by the detonation of aluminized explosive, and the after-burning combustion model was used to obtain the released energy caused by the combustion of aluminium particles. The elastic-perfectly plastic model and Tillotson equation of state were employed to predict the dynamic behavior of metal material. In addition, the density-adaptive method is employed to deal with the multiphase interface with a large density ra-

tio. Firstly, the equations of state and constitutive models are verified by two benchmark cases, namely three-dimensional detonation of PBX 9501 explosive and three-dimensional aluminium-aluminium high-velocity impact. Subsequently, the detonation velocity and peak pressure of aluminized HMX with different mass fractions of aluminium powder are investigated. In the end, the interaction between the steel confiner and the detonation of aluminized explosive is conducted in order to study the brisance performance of aluminized explosive. The numerical results obtained from smoothed particle hydrodynamics are in good agreement with the experimental data, which shows that the detonation and the ballistic performance of the condensed explosive can be captured by density-adaptive smoothed particle hydrodynamics very well.

**Keywords:** aluminized explosive · smoothed particle hydrodynamics · ignition and growth model · after-burning model

### 1 Introduction

Aluminized explosives are high explosives using micro-meter-scale aluminium (Al) particles as additive. Due to the incomplete reaction of Al at the Chapman-Jouguet (C–J) plane and after-burning of Al particles, the aluminized-explosives are characterized by reactively low brisance but high blast potential [1]. The phenomena that occurred in the detonation of the condensed explosive and the combustion of Al particles are rather complicated.

Several researchers have investigated the detonation and the brisance performance of the aluminized explosive both theoretically and experimentally. Manner et al. [2] conducted a series of cylinder tests and plate-pushing experiments to improve the understanding of how Al contributes in the detonation of non-ideal explosive mixtures, which indicates that a significant portion of Al particles reacted after the C–J plane, and continue to release energy at later times. Liu et al. [3] investigated the effects of mass fraction of Al and particle size in CL-20-based explosive on the metal acceleration and reaction characteristics by using a small-scale confined plate push test, which shows that the Al particles mainly reacted with the detonation products after the C–J point, and the released energy was used to accelerate

the metal. Liu et al. [4] studied the effects of nano-sized Al particles on detonation characteristics, detonation reaction zone, and metal acceleration for RDX-based aluminized explosives through a variety of experiments such as the detonation pressure test and the detonation velocity test. The experimental data shows that every 5% increase of gravimetric Al content results in a 1.3% decrease of the detonation velocity. Despite this effort, the use of experimentation to study the phenomenology of a detonation of aluminized explosive is rather restricted due to its prohibitive costs and difficulties in the measurement of physical phenomena occurring on very short time scales.

[a] J.-Y. Chen, G.-Y. Wang, F. Gao

School of Mechanical Engineering, Nanjing University of Science and Technology, 200 Xiaolingwei Street, Xuanwu District, Nanjing, 210094, China

\*e-mail: gwang@njust.edu.cn

[b] D.-L. Feng

Institute of Fluid Mechanics and Environmental Physics in Civil Engineering, Leibniz University Hannover, Appelstraße 9 A 30167 Hannover, Germany

[c] C. Peng

Institut für Geotechnik, Universität für Bodenkultur, Feistmantelstrasse 4, 1180 Vienna, Austria

In consequence, numerical simulation is an alternative methodology that has been applied to study the mechanism of the detonation of aluminized explosives.

The mesh-based methods, such as the finite element method, finite volume method, and finite difference method, are widely applied in the simulations of explosive detonation. Souers et al. [5] conducted the simulation of prompt detonation of ammonium nitrate/fuel oil (ANFO) K1 using the arbitrary Lagrangian-Eulerian (ALE) method with a simple reactive flow model JWL++, which consists of an unreacted equation of state (EOS), reacted EOS, and a mixer for the two EOSs. The numerical results showed that the size effect and detonation front curvature can be reproduced by using this model. Tarver and McGuire [6] investigated the shock initiation and detonation of the triamino-trinitrobenzene (TATB) based high explosives LX-17, polymer-bonded explosive (PBX) 9502 using the ALE method. Tarver et al. [7] simulated the octogen (HMX)/TATB detonation using the ignition and growth (I & G) model and compared the numerical results with the experiment conducted by Anderson et al. [8]. Kim et al. [9] studied the effects of Al fraction in a condensed explosive on the ballistic and brisance performance using a two-phase model. However, the large deformation generated by the explosive detonation may provoke mesh distortion or even computational termination. Compared to the grid-based methods, the mesh-free smoothed particle hydrodynamics (SPH) methodology is a Lagrangian particle method, and it is capable of capturing the large deformation generated by the high explosive detonation.

The smoothed particle hydrodynamics (SPH) is a methodology for obtaining numerical solutions of the governing equations of fluid dynamics by replacing the fluid with a set of particles. It was originally proposed by Gingold and Monaghan [10] and Lucy [11] independently to tackle the problems in astrophysics, and then it was extended to the applications in the field of explosion and high-velocity impact. Liu et al. [12] incorporated the Jones-Wilkins-Lee (JWL) EOS in SPH to investigate the one-dimensional (1D) Trinitrotoluene (TNT) slab detonation and 2D underwater explosion. It has shown that the SPH methodology can give a good prediction for both the magnitude and form of the detonation wave. Yang et al. [13] studied the feasibility of the SPH method combined with the I & G model in the simulation of 1D condensed explosive detonation, which provides a good prediction for the von Neumann spike state. Wang et al. [14] incorporated the JWL++ EOS in SPH to simulate the detonation of ANFO, and good agreements can be observed between experiment and SPH simulation. Furthermore, Wang et al. [15] also incorporated the afterburning model for the combustion of Al particles and simulated the 1D aluminized explosive detonation, and the numerical results showed that the SPH solver is capable of predicting the combustion of Al particles. Currently, most of the models used in the simulations of explosive detonation are either JWL or JWL++. The JWL model is rather simple

and easy to implement in a SPH solver, but it can only predict C-J state of an explosive detonation. Although the JWL++ model can reproduce the size effect of the explosive and the detonation front curvature, this model fails to predict the von Neumann spike state generated by the detonation of condensed explosives. Compared to the JWL and JWL++ EOSs, the I & G model is more accurate for the prediction of shock wave propagation caused by non-ideal explosive detonation. The ignition and growth (I & G) model describes shock initiation, the ignition of a small fraction of explosive, and the growth of reaction rate which is controlled by the pressure and the surface area as in a deflagration process [16].

In comparison with previous research, the I & G model is implemented in our graphics processing unit (GPU)-accelerated SPH solver to simulate the detonation of 3D HMX explosive involving millions of particles. Secondly, instead of using the cubic-spline function, the Wendland function is employed as the smoothing function to prevent the penetration of the particles in SPH. Thirdly, although the 3D detonation of the non-ideal explosive ANFO has been simulated using the SPH methodology, the simulation of the interaction between the non-ideal explosive detonation and the metal material involving large deformations is still in its infancy. Furthermore, the afterburning model has been introduced within the SPH framework for the first time to study the effect of different mass fractions of Al particles on the detonation and brisance performance of 3D non-ideal explosives.

The paper is organized into seven sections. A brief introduction of the SPH methodology is presented in Section 2. The EOSs and constitutive models are described in Section 3. Numerical validations of two benchmark problems, namely PBX 9501 explosive detonation and Al-Al high-velocity impact, are presented in Section 4. The detonation of the aluminized explosive and the ballistic performance of the aluminized HMX are investigated in Section 5 and Section 6, respectively. The conclusions and novelties are summarized in Section 7.

## 2 Fundamentals of the SPH Methodology

### 2.1 Function Approximation in SPH

In the SPH formulation, a state variable  $f(\mathbf{x})$  can be approximated at any spatial coordinate  $\mathbf{x}'$  through the integral,

$$\langle f(\mathbf{x}) \rangle = \int_{\Omega} f(\mathbf{x}') W(\mathbf{x} - \mathbf{x}', h) d\mathbf{x}'. \quad (1)$$

Similarly, the derivative of the state variable can be obtained as

$$\langle \nabla f(\mathbf{x}) \rangle = - \int_{\Omega} f(\mathbf{x}') \nabla W(\mathbf{x} - \mathbf{x}', h) d\mathbf{x}' , \quad (2)$$

where  $W$  is the smoothing function;  $h$  is the smoothing length. A variety of smoothing functions such as cubic spline function and gauss function have been used in SPH for simulations of large deformation problems. In our current research, the Wendland  $C^2$  function which can prevent the particles penetration has been employed in SPH [17].

$$W(q, h) = \alpha_d \begin{cases} \left(1 - \frac{q}{2}\right)^4 (2q + 1) & 0 \leq q < 2 ; \\ 0 & q \geq 2 . \end{cases} \quad (3)$$

where the normalization constant  $\alpha_d = 7/(4\pi h^2)$  in two dimensions and  $\alpha_d = 21/(16\pi h^3)$  in three dimensions;  $q = \frac{|\mathbf{x}|}{h}$  is the normalized distance. For the simulations of explosive detonation involving large deformations, the change rate of the smoothing length  $h$  is calculated by the following equation [18],

$$\frac{dh_i}{dt} = -\frac{1}{d\rho_i} \frac{h_i d\rho_i}{dt} . \quad (4)$$

It can be observed that the smoothing length  $h_i$  increases with the reduction of the particle density  $\rho_i$ , so that more particles will be involved in computation in regions with small particle density. In a SPH discretization, a material is represented by a collection of particles, each with an associated velocity, density, smoothing length, and other physical variables. Then the integral can be approximated further and becomes a summation over the particles whose smoothing function contribution is non-zero. Interpolating  $f(\mathbf{x}_i)$  or  $\nabla f(\mathbf{x}_i)$  obtains,

$$\langle f(\mathbf{x}_i) \rangle = \sum_{j=1}^N f(\mathbf{x}_j) W_{ij} \frac{m_j}{\rho_j} ; \quad (5)$$

$$\langle \nabla f(\mathbf{x}_i) \rangle = - \sum_{j=1}^N f(\mathbf{x}_j) \nabla W_{ij} \frac{m_j}{\rho_j} . \quad (6)$$

The Navier-Stokes equation is used as the governing equation for the simulation of explosive detonation.

$$\begin{cases} \frac{d\rho}{dt} = -\rho \frac{\partial v^\beta}{\partial x^\beta} , \\ \frac{dv^\alpha}{dt} = \frac{1}{\rho} \frac{\partial \sigma^{\alpha\beta}}{\partial x^\beta} , \\ \frac{de}{dt} = \frac{\sigma^{\alpha\beta}}{\rho} \frac{\partial v^\alpha}{\partial x^\beta} . \end{cases} \quad (7)$$

Based on the integral approximation and kernel approximation in SPH, the discretized governing equation can be derived as follows,

$$\begin{cases} \frac{d\rho_i}{dt} = \sum_{j=1}^N m_j v_{ij}^\alpha \cdot \frac{\partial W_{ij}}{\partial x_i^\alpha} & (a) \\ \frac{dv_i^\alpha}{dt} = \sum_{j=1}^N m_j \left( \frac{\sigma_i^{\alpha\beta} + \sigma_j^{\alpha\beta}}{\rho_i \rho_j} + \Pi_{ij} \delta^{\alpha\beta} \right) \frac{\partial W_{ij}}{\partial x_i^\beta} & (b) \\ \frac{de_i}{dt} = \frac{1}{2} \sum_{j=1}^N m_j \frac{\rho_i + \rho_j}{\rho_i \rho_j} v_{ij}^\beta \cdot \frac{\partial W_{ij}}{\partial x_i^\beta} + \frac{1}{2\rho_i} S_i^{\alpha\beta} \varepsilon_i^{\alpha\beta} & (c) \\ p_i = p(\rho_i, e_i) & (d) \end{cases} \quad (8)$$

where  $\rho_i$ ,  $m_i$ ,  $v_i$ ,  $e_i$  and  $p_i$  are the density, mass, velocity, energy, and pressure of particle  $i$ , respectively;  $\Pi_{ij}$  is artificial viscosity;  $\sigma$  is stress tensor;  $S$  is deviatoric stress tensor.

To dampen the pressure fluctuations, irregular particle motion, and to prevent non-physical collisions of two approaching particles, the Monaghan-type artificial viscosity is employed in SPH [19]. The artificial viscosity term included in the momentum equation is represented as follows,

$$\Pi_{ij} = \begin{cases} \frac{-\alpha c_{ij} \phi_{ij} + \beta \phi_{ij}^2}{\rho_{ij}} , & \mathbf{v}_{ij} \cdot \mathbf{x}_{ij} < 0 ; \\ 0 , & \mathbf{v}_{ij} \cdot \mathbf{x}_{ij} \geq 0 . \end{cases} \quad (9)$$

Here,  $\phi_{ij} = \frac{h_{ij} \mathbf{v}_{ij} \cdot \mathbf{x}_{ij}}{|\mathbf{x}_{ij}|^2 + (\varphi)^2}$ ,  $c_{ij} = \frac{1}{2}(c_i + c_j)$ ,  $\rho_{ij} = \frac{1}{2}(\rho_i + \rho_j)$ ,  $h_{ij} = \frac{1}{2}(h_i + h_j)$ ,  $\mathbf{v}_{ij} = \mathbf{v}_i - \mathbf{v}_j$ , and  $\mathbf{x}_{ij} = \mathbf{x}_i - \mathbf{x}_j$ , where  $\alpha$  and  $\beta$  are tuning parameters depending on the problem;  $c_i$  is the sound speed associated with particle  $i$ ;  $\varphi = 0.1 h_{ij}$  is used to prevent numerical divergence when two particles approach one another. Although artificial viscosity can reduce pressure fluctuations, it is unable to eliminate them.

## 2.2 The Treatment of Multiphase Interface with High-Density Ratio

The treatment of the multiphase interface between metal material and explosive gaseous products which involves a high-density ratio is an important issue in SPH. Monaghan et al. indicates that the simulation of the multiphase flow using the conventional SPH method may invoke numerical instability or even computational termination [20]. There are two conventional methods for the calculation of density. One approach is

$$\frac{d\rho_i}{dt} = \sum_{j=1}^N m_j \left( v_i^\alpha - v_j^\alpha \right) \frac{\partial W_{ij}}{\partial x_i^\alpha} , \quad (10)$$

another one is

$$\frac{d\rho_i}{dt} = \rho_i \sum_{j=1}^N \frac{m_j}{\rho_j} (\nu_i^a - \nu_j^a) \frac{\partial W_{ij}}{\partial x_i^a}, \quad (11)$$

In practice, Monaghan found that either Eq. 10 or Eq. 11 can be used for density ratio  $\leq 2$ , but large density ratio, it is better to use Eq. 11 [20]. To tackle the multiphase interface with a large density ratio, the modified equation for the density calculation has been proposed by Liu et al. [21] through a combination of Eq. 10 and Eq. 11.

$$\frac{d\rho_i}{dt} = \sum_{j=1}^N \frac{\rho_i + \psi_i \rho_j}{(1 + \psi_i) \rho_j} m_j \nu_{ij}^a \cdot \frac{\partial W_{ij}}{\partial x_i^a}, \quad (12)$$

in which,

$$\psi_i = \frac{1}{ln k_i}, \quad (13)$$

$$k_i = \frac{\rho_{i,max}}{\rho_{i,min}}. \quad (14)$$

$i,max$  and  $i,min$  denote the particles with maximum density and minimum density within the support domain associated with particle  $i$ , respectively.

### 2.3 Explicit Time Integration

In the SPH method, the physical variables can be updated by using the explicit integration methods, e.g. the leap-frog method, the valet method, and the predictor-corrector method. In our current research, the predictor-corrector numerical scheme has been employed in SPH for the update of position, velocity, density, and stress tensor associated with each particle [22]. In the prediction step, the physical variables at half time step can be predicted as

$$\mathbf{x}_i^{t+\frac{\Delta t}{2}} = \mathbf{x}_i^t + \frac{\Delta t}{2} \mathbf{v}_i^t, \quad (15)$$

$$\mathbf{v}_i^{t+\frac{\Delta t}{2}} = \mathbf{v}_i^t + \frac{\Delta t}{2} \mathbf{a}_i^t, \quad (16)$$

$$\rho_i^{t+\frac{\Delta t}{2}} = \rho_i^t + \frac{\Delta t}{2} \left( \frac{d\rho_i}{dt} \right)^t, \quad (17)$$

and

$$\sigma_i^{t+\frac{\Delta t}{2}} = \sigma_i^t + \frac{\Delta t}{2} \left( \frac{d\sigma_i}{dt} \right)^t, \quad (18)$$

where  $\Delta t$  is the time step and the superscript  $t$  is the time at the beginning of the computational step; In the corrector

step, the physical variables at the end of the computational step can be obtained by using the following equations.

$$\mathbf{x}_i^{t+\Delta t} = \mathbf{x}_i^t + \Delta t \mathbf{v}_i^{t+\frac{\Delta t}{2}}, \quad (19)$$

$$\mathbf{v}_i^{t+\Delta t} = \mathbf{v}_i^t + \Delta t \mathbf{a}_i^{t+\frac{\Delta t}{2}}. \quad (20)$$

and

$$\rho_i^{t+\Delta t} = \rho_i^t + \Delta t \left( \frac{d\rho_i}{dt} \right)^{t+\frac{\Delta t}{2}}, \quad (21)$$

In the corrector step, the components of the stress tensor are updated based on the value of the stress tensor obtained from the end of the prediction step (half-time step), to simplify the computation and reduce the storage required in GPU memory.

$$\sigma_i^{t+\Delta t} = \sigma_i^{t+\frac{\Delta t}{2}} + \frac{\Delta t}{2} \left( \frac{d\sigma_i}{dt} \right)^{t+\frac{\Delta t}{2}}. \quad (22)$$

## 3 EOSs and Constitutive Models

### 3.1 Ignition and Growth Model

The I & G reactive flow model uses two Jones-Wilkins-Lee (JWL) equations of state in the form [7]:

$$\begin{cases} p_s = A_s e^{-R_{1s} V_s} + B_s e^{-R_{2s} V_s} + w_s C_{vs} T_s / V_s; & (a) \\ p_g = A_g e^{-R_{1g} V_g} + B_g e^{-R_{2g} V_g} + w_g C_{vg} T_g / V_g. & (b) \end{cases}$$

where  $p$  is pressure; the subscripts  $s$  and  $g$  denote solid and gas state, respectively;  $T$  is the temperature;  $C_v$  is the average heat capacity;  $V$  is volume ratio;  $A$ ,  $B$ ,  $R_1$ ,  $R_2$ , and  $w$  are parameters fitted to experiments.

Initially, the explosive is in a solid-state. After the impaction, the solid explosive is ignited and transferred to the solid and gas mixtures. It is assumed that each explosive particle consists of solid phase and gas phase (see Figure 1), and thus two physical assumptions are introduced for the mixtures of solid explosive and gaseous explosive product, i.e., the pressure equilibrium equation  $p_g = p_s$  and temperature equilibrium equation  $T_s = T_g$  [23]. The temperature of the mixture can be calculated using the following equation,

$$T_s = T_g = \frac{E}{C_v} = \frac{E}{(1-F)C_{vs} + FC_{vg}}, \quad (24)$$

where  $E$  is the specific internal energy;  $C_v$ ,  $C_{vs}$ , and  $C_{vg}$  are the specific heat of the mixture, solid explosive, and gaseous products, respectively.  $F$  is the reacted fraction. As the mass of each particle is a constant, the mass fraction of each phase can be determined following these two assumptions. The reaction rate  $\frac{dF}{dt}$  is calculated by

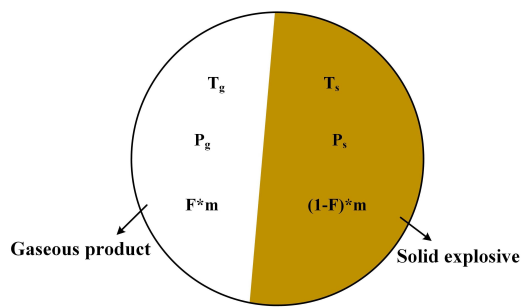


**Figure 1.** The pressure equilibrium, temperature equilibrium, and reaction rate of the solid explosive (unreacted region) and its gaseous products (reacted region), in which  $m$  is the mass of a given particle.

$$\frac{dF}{dt} = I(1 - F)^b \left( \frac{\rho}{\rho_0} - 1 - a \right)^x + G_1(1 - F)^c F^d p^y \\ + G_2(1 - F)^e F^g p^z, \quad (25)$$

$0 < F < \lambda_{igmax}$        $0 < F < \lambda_{G1max}$

$\lambda_{G2min} < F < 1$

where  $t$  is time;  $\rho$  is the current density;  $\rho_0$  is the initial density.  $I$ ,  $G_1$ ,  $G_2$ ,  $x$ ,  $y$ ,  $z$ ,  $a$ ,  $b$ ,  $c$ ,  $d$ ,  $e$ ,  $g$ ,  $\lambda_{igmax}$ ,  $\lambda_{G1max}$  and  $\lambda_{G2max}$  are parameters fitted to experiments. The reacted fraction  $F$  ranges from 0 to 1, and it can be determined using time integration. The explosive is in a solid-state when  $F = 0$ , and  $F = 1$  denotes a full reaction of the explosive.

### 3.2 Afterburning Model for the Combustion of Aluminized Particles

Several researchers have conducted an experimental and numerical analysis to investigate the mechanism of the combustion of the Al particles. Boiko and Poplavski [24] investigated the combustion of the Al particles in the propagation of shock waves. Kuhl et al. [25] proposed a heterogeneous continuum model for the simulation of an

explosion of aluminized explosives. Compared to the previous combustion models, the afterburning model proposed by Miller [26] is simple and easy to implement in SPH. In consequence, the EOS for the detonation of aluminized explosive should be modified as

$$p = Ae^{-R_1 V} + Be^{-R_2 V} + w(C_v T + \alpha^* Q)/V, \quad (26)$$

where  $Q$  is the total energy generated by the combustion of aluminized particles. The change rate of the combustion process  $\alpha$  can be obtained by using the following equation,

$$\frac{d\alpha}{dt} = a(1 - \alpha)^{1/2} \left( \frac{p}{p_0} \right)^{1/6}, \quad (27)$$

where the constant-coefficient  $a$  is set as 1950;  $p_0$  is the atmospheric pressure. As the combustion of aluminized particles is much slower than explosive detonation, it is assumed that the combustion of aluminized particles only happens to the SPH particles that are in the full gas state, i.e., the combustion of Al powder is only considered in Eq. 23(b).

As shown in Figure 2, the heterogeneous aluminized explosive is considered as two homogeneous materials. The diluted densities in each space are determined based on the mass fraction ( $a$ ) of Al in aluminized explosive, the density of HMX  $\rho_{HMX}$ , and the density of Al particles.

$$\frac{V_a \rho_{Al}}{(1 - V_a) \rho_{HMX}} = \frac{a}{(1 - a)} - , \quad (28)$$

$$\rho_0 = (1 - V_a) \rho_{HMX}, \quad (29)$$

$$\rho_{A0} = V_a \rho_{Al}. \quad (30)$$

where  $\rho_0$  represents the initial diluted density of explosives, and  $\rho_{A0}$  is the initial diluted density of Al particles.

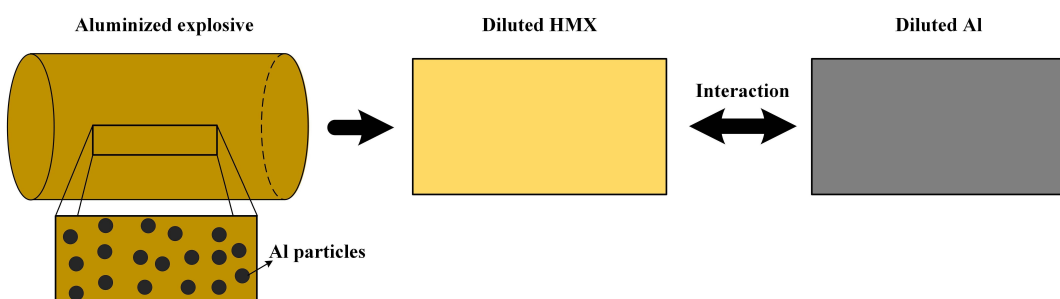


**Figure 2.** The structure of the heterogeneous aluminized explosive model.

### 3.3 Tillotson EOS

The Tillotson EOS is employed to calculate the pressure of the metal material [27], and this EOS is divided into four regions in accordance to the specific energy and compression  $\mu = \eta - 1$ , in which  $\eta = \frac{\rho}{\rho_0}$ .

1) If the compression  $\mu \geq 0$ , the pressure is calculated by the following equation,

$$p_1 = (a + \frac{b}{w_0})\eta\rho_0E + A\mu + B\mu^2; \quad (31)$$

2) If  $\mu \geq 0$  and  $E \leq E_s$ , the pressure is determined by

$$p_2 = \left(a + \frac{b}{w_0}\right)\eta\rho_0E + A\mu; \quad (32)$$

3) If  $\mu \geq 0$  and  $E_s \leq E \leq E'_s$ , the pressure is calculated by

$$p_3 = p_2 + (p_4 - p_2)\frac{E - E_s}{E'_s - E_s}; \quad (33)$$

4) If  $\mu \geq 0$  and  $E \geq E'_s$ , the pressure can be obtained as

$$p_4 = a\eta\rho_0E + \left(\frac{b\eta\rho_0E}{w_0} + A\mu e^{\beta x}\right)e^{-\alpha x}. \quad (34)$$

where  $w_0 = 1 + \frac{E}{E_0\eta^2}$ ,  $E_s$ ,  $E'_s$ ,  $E_0$ ,  $A$ ,  $B$ ,  $a$ ,  $b$ ,  $\alpha$ ,  $\beta$  are the property coefficients of materials. The pressure is assumed to be 0 Pa when the material is in the tensile state.

### 3.4 Elastic-Perfectly Plastic Constitutive Model

To simulate the dynamic behavior of metal material, the elastic-perfectly plastic constitutive model is implemented within SPH. An objective stress rate Jaumann rate of the Cauchy stress which does not depend on the frame of reference is used in this constitutive model [28].

$$\dot{S}^{ab} = \dot{S}_J^{ab} + S^{ay}\dot{w}^{by} + S^{yb}\dot{w}^{ay}. \quad (35)$$

In the elastic range, Hooke's law is applied,

$$\dot{S}_J^{ab} = 2G\left(\dot{\varepsilon}^{ab} - \frac{1}{3}\delta^{ab}\dot{\varepsilon}^{\gamma\gamma}\right), \quad (36)$$

in which  $G$  is the shear modulus of materials. The components of trial elastic deviatoric stress  $S_e^{ab}$  can be updated by substituting Eq. (36) to Eq. (35),

$$\begin{aligned} S_e^{ab} = \Delta t &\left(2G\left(\dot{\varepsilon}^{ab} - \frac{1}{3}\delta^{ab}\dot{\varepsilon}^{\gamma\gamma}\right) + S^{ay}\dot{w}^{by} + S^{yb}\dot{w}^{ay}\right) \\ &+ S_{(n)}^{ab}, \end{aligned} \quad (37)$$

where  $S_{(n)}^{ab}$  is the component of deviatoric stress at the n-th time step. The strain rate tensor  $\dot{\varepsilon}^{ab}$  and spin rate tensor  $\dot{w}^{ab}$  are defined in the following,

$$\dot{\varepsilon}^{ab} = \frac{1}{2}\left(\frac{\partial v^a}{\partial x^\beta} + \frac{\partial v^\beta}{\partial x^a}\right) \quad (38)$$

and

$$\dot{w}^{ab} = \frac{1}{2}\left(\frac{\partial v^a}{\partial x^\beta} - \frac{\partial v^\beta}{\partial x^a}\right). \quad (39)$$

The discretized forms of the strain rate tensor and spin rate tensor can be derived using the SPH methodology,

$$\dot{\varepsilon}_i^{ab} = \frac{1}{2}\sum_{j=1}^N \frac{m_j}{\rho_j} \left(v_{ji}^\alpha \frac{\partial W_{ij}}{\partial x_i^\beta} + v_{ji}^\beta \frac{\partial W_{ij}}{\partial x_i^\alpha}\right) \quad (40)$$

and

$$\dot{w}_i^{ab} = \frac{1}{2}\sum_{j=1}^N \frac{m_j}{\rho_j} \left(v_{ji}^\alpha \frac{\partial W_{ij}}{\partial x_i^\beta} - v_{ji}^\beta \frac{\partial W_{ij}}{\partial x_i^\alpha}\right) \quad (41)$$

where  $v_{ji}^\alpha = v_j^\alpha - v_i^\alpha$ . The second invariant  $J_2$  of the deviatoric part of the elastic trial stress  $S_e^{ab}$  is

$$J_2 = \frac{1}{2}S_e^{ab}S_e^{ab}. \quad (42)$$

The metal material is still in the elastic range if  $J_2$  is less than one-third of the square of the yield stress  $\sigma_Y$ ; otherwise, the material is in the plastic range and is determined by using the classic radial return algorithm.

$$S^{ab} = \begin{cases} S_e^{ab}, & \text{if } J_2 \leq \sigma_Y^2/3; \\ \sqrt{\frac{\sigma_Y^2}{3J_2}}S_e^{ab}, & \text{if } J_2 > \sigma_Y^2/3. \end{cases} \quad (43)$$

A temperature-dependent viscoplastic model (Johnson-Cook model) suitable for high strain rates is used to determine the yield stress  $\sigma_Y$  of metal material,

$$\sigma_Y = [A + B(\varepsilon_p)^n] \left[1 + C \ln\left(\frac{\dot{\varepsilon}_p}{\dot{\varepsilon}_0}\right)\right] \left[1 - (T^*)^k\right], \quad (44)$$

where  $A$  is the yield stress at room temperature;  $B$  is the hardening modulus;  $C$  is the strain rate hardening co-

efficient.  $n$  and  $k$  denote work hardening and thermal softening, respectively.  $\varepsilon_p$  is plastic strain;  $\dot{\varepsilon}_p$  is effective strain rate;  $\dot{\varepsilon}_0 = 1\text{s}^{-1}$  is reference strain rate. The dimensionless temperature  $T^*$  is determined by

$$T^* = \frac{T - T_{\text{room}}}{T_{\text{melt}} - T_{\text{room}}}, \quad (45)$$

where  $T$ ,  $T_{\text{room}}$ , and  $T_{\text{melt}}$  are temperature, room temperature, and melt temperature, respectively. The incremental plastic work of metal material is determined by

$$\Delta W_p^{(n)} = \frac{1}{2} \left( \sigma_p^{(n+1)} + \sigma_p^{(n)} \right) \Delta \varepsilon_p^{(n)} \left( \frac{m}{\rho^{(n+1/2)}} \right), \quad (46)$$

where  $\sigma_p$  at the  $(n+1)$ -th time step is calculated from the deviatoric stress tensor  $S_e^{(n+1)}$  as follows:

$$\sigma_p^{(n+1)} = \left( \frac{3}{2} S_e^{(n+1)} : S_e^{(n+1)} \right)^{1/2}. \quad (47)$$

The incremental plastic strain is determined by

$$\Delta \varepsilon_p^{(n)} = \frac{\sigma_p^{(n)} - \sigma_Y}{3G}. \quad (48)$$

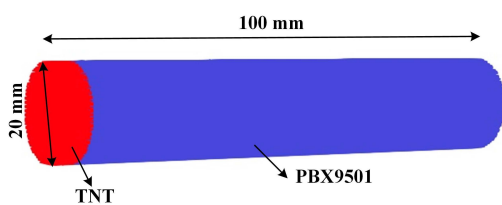


**Figure 3.** The initial geometry of the 3D PBX 9501 explosive.

**Table 1.** Reaction rate parameters for the detonation of PBX 9501 [29].

$I$	$1.4 \times 10^{17} \text{ s}^{-1}$	$g$	1.0
$a$	0.0	$z$	2.0
$b$	0.667	$G_1$	$1.3 \times 10^{-14} \text{ Pa}^{-y} \text{s}^{-1}$
$x$	20.0	$G_2$	$4.0 \times 10^{-14} \text{ Pa}^{-z} \text{s}^{-1}$
$c$	0.667	$\lambda_{G1max}$	0.3
$d$	0.277	$\lambda_{G1max}$	0.5
$y$	2.0	$\lambda_{G2max}$	0.5
$e$	0.333		

**Table 2.** Coefficients of the JWL model for the solid and gaseous products of PBX 9501 [29].

	$\rho_0 (\text{kg m}^{-3})$	$A (\text{Pa})$	$B (\text{Pa})$	$R1$	$R2$	$w$	$Cv (\text{J} / (\text{m}^3 \cdot \text{K}))$
Unreacted PBX 9501	1,835	$7.32 \times 10^{14}$	$-5.26 \times 10^9$	14.1	1.41	0.8867	$2.78 \times 10^6$
Reacted PBX 9501	1,835	$1.6689 \times 10^{12}$	$5.969 \times 10^{10}$	5.9	2.1	0.45	$1.0 \times 10^6$

## 4 Numerical Validation

### 4.1 PBX 9501 Explosive Detonation

The simulation of 3D PBX 9501 explosive detonation is conducted to validate the I&G model. PBX 9501 explosive, which consists of 95% HMX, 2.5% estane binder, and 2.5% BDNPA/F, is a HMX-based bonded explosive. As shown in Figure 3, the diameter and length of PBX 9501 are 20 mm and 100 mm, respectively. A length of 2 mm TNT explosive is located at the left end of the PBX 9501 so that the PBX 9501 will be ignited by the detonation of the TNT explosive. The parameters of I&G model for PBX 9501 are summarized in Tables 1 and 2. The initial particle spacing was  $\Delta x = 0.4$  mm, and a total of 509,590 particles were involved in this numerical case. The initial smoothing length was  $1.5 \times \Delta x = 0.6$  mm. To confirm the computational stability of this simulation, the time step for this case was set as  $\Delta t = 1.0 \times 10^{-9}$  s.

The temporal evolution of velocity distributions of the 3D PBX 9501 detonation at following times 1  $\mu\text{s}$ , 4  $\mu\text{s}$ , 8  $\mu\text{s}$ , and 12  $\mu\text{s}$  are displayed in Figure 4. When the PBX 9501 is ignited by the detonation of TNT, the detonation shock wave is generated by the impaction and propagates along with the slab of 3D PBX 9501 explosive (Figure 4 (a)). Then the gaseous product generated by the explosive detonation expands outwards. The detonation velocity increases gradually with the detonation of PBX 9501 explosive. After 5  $\mu\text{s}$  of ignition, the detonation of the PBX 9501 explosive reaches a steady-state, and it is found that the numerical velocity of the shock wave propagation at a steady state is  $8,400 \text{ m s}^{-1}$ , which agrees well with the experimental detonation velocity  $8,800 \text{ m s}^{-1}$  in [30]. The temporal evolution of the pressure distributions of the PBX 9501 at following times 1  $\mu\text{s}$ , 4  $\mu\text{s}$ , 8  $\mu\text{s}$ , and 12  $\mu\text{s}$  are shown in Figure 5, and it can be observed that the pressure magnitude reaches the largest value at the centerline of the slab. The numerical peak pressure are compared against the experimental data [29], and it is seen that the numerical peak pressure 39 GPa is close to the experimental peak pressure 39.5 GPa (see Figure 6). Since the detonation process is rather complex, the numerical model is limited to describing all the reaction details. This numerical case shows that the SPH methodology coupled with the I&G model can reproduce the propagation of the detonation wave and predict the pressure distribution of non-ideal explosive detonation very well.

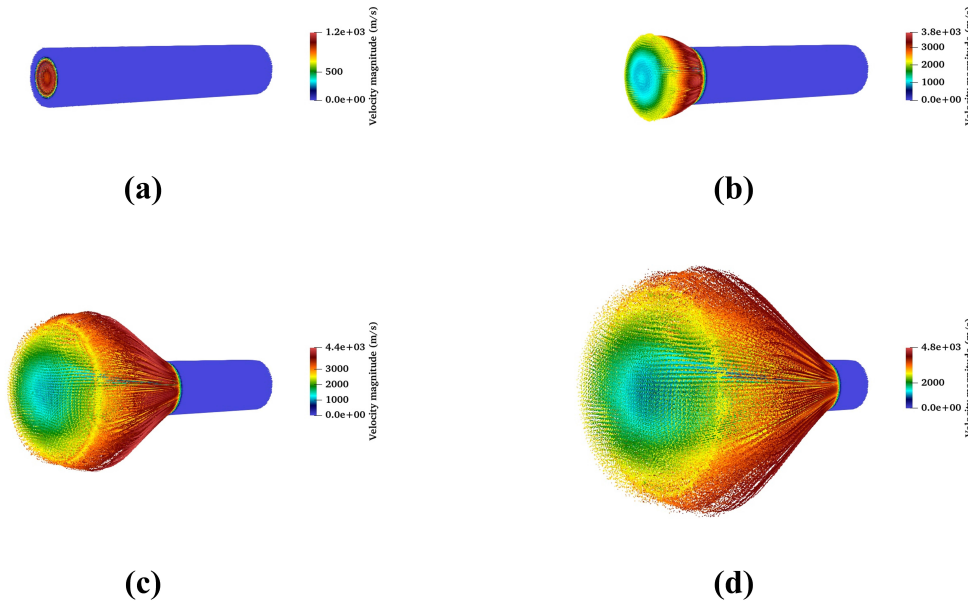


**Figure 4.** The temporal evolution of velocity distribution of the detonation of PBX 9501 at four different times, namely at (a) 1  $\mu$ s, (b) 4  $\mu$ s, (c) 8  $\mu$ s, and (d) 12  $\mu$ s.

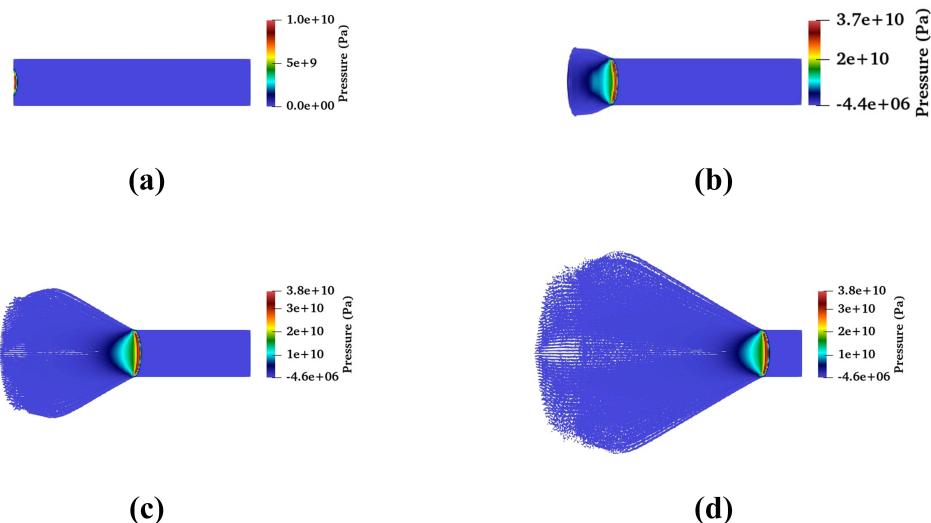


**Figure 5.** The temporal evolution of pressure distribution of the detonation of PBX 9501 at four different times, namely at (a) 1  $\mu$ s, (b) 4  $\mu$ s, (c) 8  $\mu$ s, and (d) 12  $\mu$ s.

#### 4.2 3D Al-Al High-Velocity Impact

To verify the Tillotson EOS and elastic-perfectly plastic constitutive model, the simulation of the impact of the 3D aluminum (Al) sphere on a thin Al plate has been conducted. As shown in Figure 7, the initial velocity of the Al sphere is  $6810 \text{ m s}^{-1}$ . The initial length, width, and height of the Al

plate are 100 mm, 4 mm, 100 mm, respectively, and the radius of the Al sphere is 5 mm. The initial particle spacing was set as 0.4 mm, and a total number of 690,165 particles were employed in this simulation. The parameters of the Johnson-Cook model and Tillotson EOS for Al-Al high-velocity impact are shown in Tables 3 and 4, respectively. The time step was  $1 \times 10^{-8} \text{ s}$  in this numerical case.

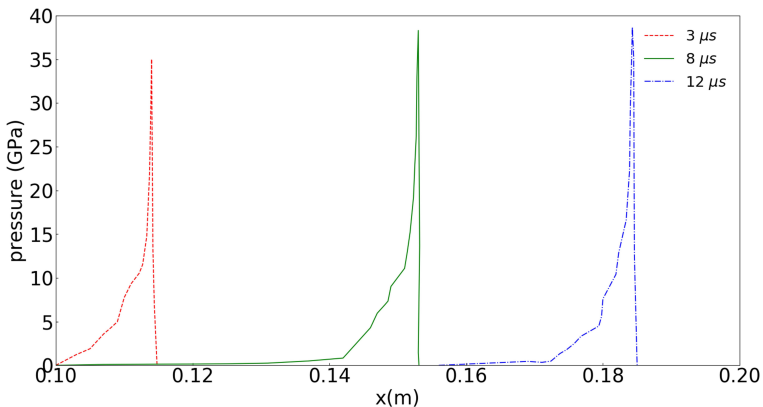


**Figure 6.** The pressure distributions along the centerline of the 3D PBX 9501 explosive slab at 3  $\mu$ s, 8  $\mu$ s, and 12  $\mu$ s.

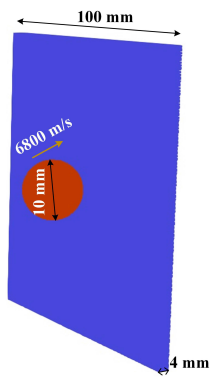


**Figure 7.** The initial configuration of the Al-Al high-velocity impact.

**Table 3.** Johnson-Cook parameters for Al-Al high velocity impact [31].

A (MPa)	B (MPa)	C	n	k	T <sub>room</sub> (K)	T <sub>melt</sub> (K)
175	380	0.0015	0.34	1.0	273	775

**Table 4.** Tillotson EOS parameters for Al-Al high velocity impact [31].

A (GPa)	B (GPa)	a	b	$\alpha$	$\beta$	$E_0$ (kJ·g <sup>-1</sup> )	$E_s$ (kJ·g <sup>-1</sup> )	$E_1$ (kJ·g <sup>-1</sup> )
75.20	65.00	0.50	1.63	5.00	5.00	5.00	3.00	15.00

The predicted velocity distributions of Al-Al high-velocity impact at following times 5  $\mu$ s, 10  $\mu$ s, 15  $\mu$ s, and 20  $\mu$ s are shown in Figure 8. It can be observed that a big crater and debris cloud are generated by the impact of the Al sphere at high velocity (see Figure 8 (d)). The crater diameter and the ratio of the length to the width of the debris

cloud obtained from SPH are 3.60 cm and 1.2, respectively. Furthermore, the numerical results using SPH are compared against the experimental data conducted by Hiermaier [32]. Hiermaier et al. [32] experimented with the impact of Al spheres on thin plates of different materials. The ratio of width to the length of debris cloud and width of the crater was obtained from the current SPH methodology and Hiermaier et al. [32] are shown in Table 5. It is seen that the relative error between experimental data and numerical result is less than 14%, which shows that the SPH methodology is capable of tackling the large deformation occurring in high-velocity impact very well.

## 5 3D Detonation of Aluminized HMX Explosive

After the validation of the I&G EOS and elastic-perfectly plastic constitutive model, the effect of different mass fractions of Al particles on the detonation velocity and peak pressure of the aluminized HMX explosive will be studied. The aluminized explosive HMX-Al consists of 74% HMX, 10% Al, 7.5% GAP, 7.5% FomblinD, and 1% isonate. In this simulation, the initial configuration of HMX-Al explosive is the same as that in Figure 3. The parameters for the I&G model and afterburning model are summarized in Tables 1 and 6, respectively. The initial particle spacing was  $dx = 0.4$  mm, and a total of 509,590 particles were involved in this

**Table 5.** Comparison of the ratio of  $L$  (the length of debris cloud) to  $W$  (the width of debris cloud) and  $D_c$  (crater diameter) for 3D Al-Al high-velocity impact.

	Simulation	Experiment [32]	Relative error (%)
$L/W$	1.20	1.39	13.6
$D_c$ (cm)	3.60	3.45	4.34

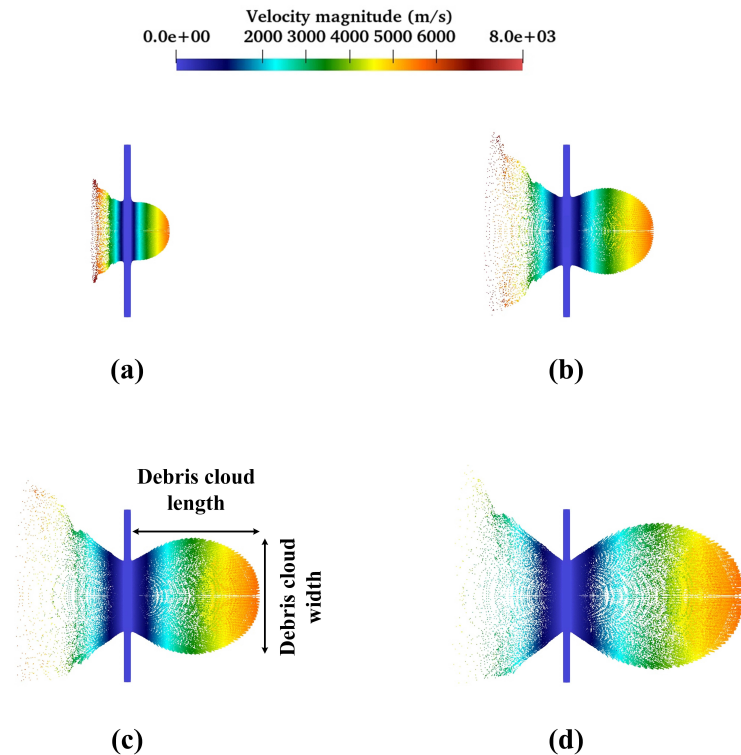


**Figure 8.** The temporal evolution of velocity distributions of 3D Al–Al high-velocity impact at different times: (a) 5  $\mu$ s, (b) 10  $\mu$ s, (c) 15  $\mu$ s, and (d) 20  $\mu$ s.

**Table 6.** Parameters of the afterburning model for the combustion of aluminized particles [14].

$Q$ (J)	$a$	$p_0$ (Pa)
$5.0 \times 10^{10}$	1950	$1.0 \times 10^5$

simulation. The initial smoothing length of the explosive particles was  $2.0 \times dx = 0.8$  mm.

The temporal evolution of the pressure distributions of 3D HMX–Al explosive at four different times, namely at 1  $\mu$ s, 4  $\mu$ s, 8  $\mu$ s, and 12  $\mu$ s, are depicted in Figure 9. It is seen that the shock wave propagates along with the slab of HMX–Al explosive, and the detonation process is similar to the detonation process of non-aluminized HMX explosive shown in Figure 5. However, the peak pressure generated by the detonation of the HMX–Al explosive is 31 GPa, which is less than the peak pressure of the non-aluminized HMX detonation 38 GPa.

In addition, the detonation velocities and peak pressures for the HMX-based aluminized explosive with different mass ratios of Al particles (5%, 7%, 10%, and 15%) are investigated and compared with these physical quantities in the detonation of non-aluminized HMX explosives. As shown in Figure 10, the shock wave propagation of the aluminized explosive with a 5% mass fraction of Al particles is

much faster than that of the aluminized explosives with more gravimetric Al content. Quantitatively, it can be observed from Figure 11 that the detonation velocity decreases from  $8,400\text{ m s}^{-1}$  to  $5114\text{ m s}^{-1}$  with the growth of mass ratios of Al particles. The rate of the decrease of velocity magnitude increases when the Al mass fraction is less than 10%; after that, the decrease rate grows gradually. Secondly, as depicted in Figure 12, the C–J pressure declines from 39 GPa to 30 GPa with the increase of the Al mass ratio, i.e., every 3% increase of the mass ratio of Al particle leads to nearly 5.5% decrease of the magnitude of peak pressure. This is because, with the increase of the Al fraction, less content of the HMX explosive is involved in the reaction of detonation. The peak pressure obtained using the SPH method is in general agreement with the numerical results from [9]. But the discrepancy between them becomes larger with the increase of Al mass fraction. This is probably because more heat energy is generated by the two-phase model in [9] than the Miller's model [26] employed in SPH. In contrast, it can be found that the pressure in the far-field (0.7 m away from the left end of the aluminized explosive slab in the horizontal direction) increases from 0.39 GPa to 0.699 GPa gradually with the rise of the mass fraction of Al particle (see Figure 13). The reason is that the combustion of Al powder is much slower than the

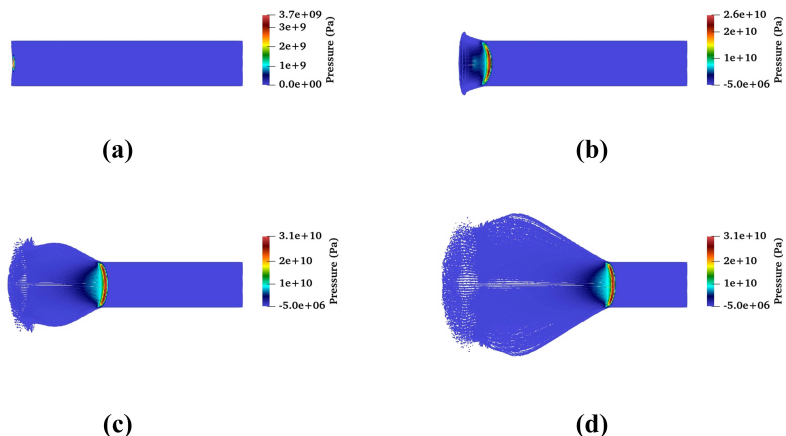


**Figure 9.** The shock wave propagation of the aluminized HMX detonation at a time of (a) 1  $\mu$ s, (b) 4  $\mu$ s, (c) 8  $\mu$ s, and (d) 12  $\mu$ s.

detonation of HMX explosive, and more energy will be released due to the combustion of Al particles at a later time. The phenomena observed from the numerical study are in good agreement with the experimental data [4], which shows that the SPH method coupled with the I & G is capable of predicting the detonation of the aluminized explosive well.

## 6 The Ballistic Performance of Aluminized HMX Explosive

The confined rate stick test with a steel confiner has been simulated to study the ballistic performance of aluminized HMX explosives. Firstly, the non-aluminized explosive detonation within a steel confiner is studied using the elastic-perfectly plastic model, Tillotson EOS, and I & G model. The initial configuration of the steel confined rate stick is depicted in Figure 14. The length and diameter of the explosive are 100 mm and 20 mm, respectively. The thickness of the confiner material is 5 mm. The initial particle spacing was 0.4 mm, and a total number of 1,038,862 particles were employed in this simulation. In addition, the initial smooth-

ing lengths of the explosive and steel were  $2.0 \times dx = 0.8$  mm and  $3.0 \times dx = 1.2$  mm, respectively. The time step was set as  $1 \times 10^{-8}$  s in this numerical case. The parameters for the constitutive model and EOSs are summarized in Tables 7, 8, and 1, respectively.

The predicted temporal evolution of the velocity distributions of the expansion of the steel shell at four different times 4  $\mu$ s, 6  $\mu$ s, 8  $\mu$ s, and 12  $\mu$ s are shown in Figure 15. The high explosive is activated at the left end of the slab, and the resulting shock wave causes the steel cylinder to rapidly expand. It can be observed that the radial velocity of the Al confiner increases to 3,700 m s<sup>-1</sup> rapidly due to the impaction of the shock wave generated by the explosive detonation.

Subsequently, the aluminized explosive with a 15% mass ratio of Al particles within a steel confiner is simulated. The initial configuration and particle spacing are the same as those in the simulation of non-aluminized explosive detonation. The coefficients of the afterburning model for the combustion of aluminized particles are listed in Table 6. The expansion process of the steel confiner is similar to that in Figure 15, but the numerical magnitude of the radial velocity of the Al confiner decreases to 2,000 m s<sup>-1</sup>. The reduction of the velocity magnitude of the steel confiner is reasonable, as the expansion of the confiner is mainly caused by the propagation of shock waves, and it can be observed from Section 5 that the peak pressure of the non-aluminized explosive is larger than aluminized explosive. However, as depicted in Figure 13, the velocity of steel confiner will continue to rise gradually due to the released energy generated by the combustion of Al particles. The numerical results show that the SPH methodology is capable of predicting the interaction between the steel confiner and non-ideal explosive detonation and the expansion of the cylindrical steel confiner involving large deformations very well.

**Table 7.** Johnson-Cook model parameters of steel [31].

A (MPa)	B (MPa)	C	n	k	T <sub>room</sub> (K)	T <sub>melt</sub> (K)
350	275	0.022	0.36	1.00	273	1810

**Table 8.** Tillotson EOS parameters for steel [31].

A (GPa)	B (GPa)	a	b	$\alpha$	$\beta$	$E_0$ (kJ g <sup>-1</sup> )	$E_s$ (kJ g <sup>-1</sup> )	$E^1$ (kJ g <sup>-1</sup> )
127.90	105.00	0.50	1.63	5.00	5.00	9.50	2.44	10.20

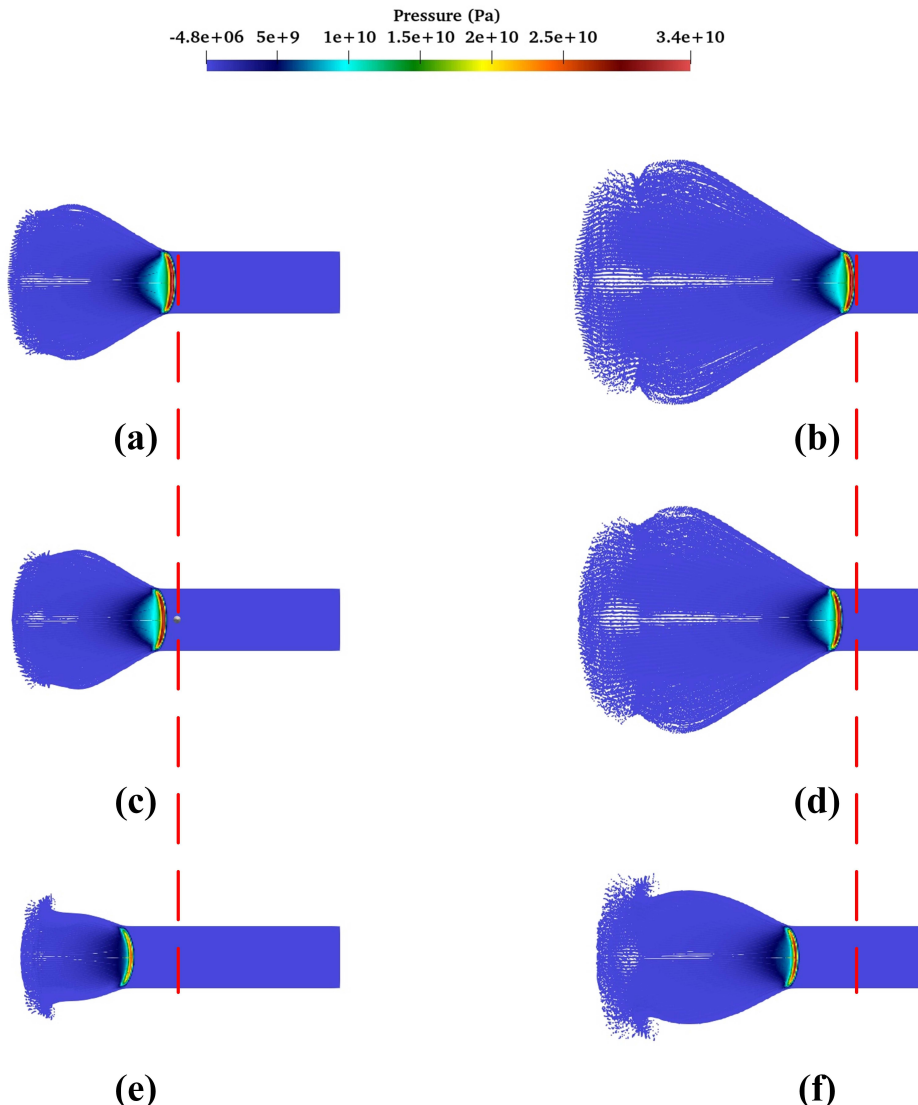


**Figure 10.** The pressure distributions of the aluminized explosive with different mass fractions of Al particles: (a,b) 5%, (c,d) 7%, and (e,f) 15% at 8  $\mu$ s (a, c, and e) and 12  $\mu$ s (b, d, and f).

## 7 Conclusion

In this paper, the I&G EOS and afterburning model have been incorporated in SPH to calculate the pressure and released energy generated by the detonation of aluminized HMX, and the elastic-perfectly plastic model and Tillotson EOS are employed to predict the dynamic behavior of metal material. Firstly, the EOSs and constitutive models are verified by the 3D detonation of PBX 9501 explosive and 3D Al-Al high-velocity impact. Then the detonation process of aluminized explosives with different mass fractions of Al particles is investigated. At the end, the ballistic performance of the aluminized HMX has been studied using the

density-adaptive SPH methodology. Some conclusions and novelties are summarized as follows,

- The 3D detonation of aluminized HMX involving millions of particles has been simulated for the first time using the I & G model within the SPH framework. The peak pressure and the expansion of the gaseous products generated by the detonation of this condensed explosive have been captured by SPH.
- The influence of different Al mass fractions on the magnitudes of the detonation velocity and peak pressure of 3D aluminized HMX explosive has been studied using SPH. It is seen that both the peak pressure and detonation velocity generated by the detonation of the aluminized HMX explosive decrease with the growth of the Al mass

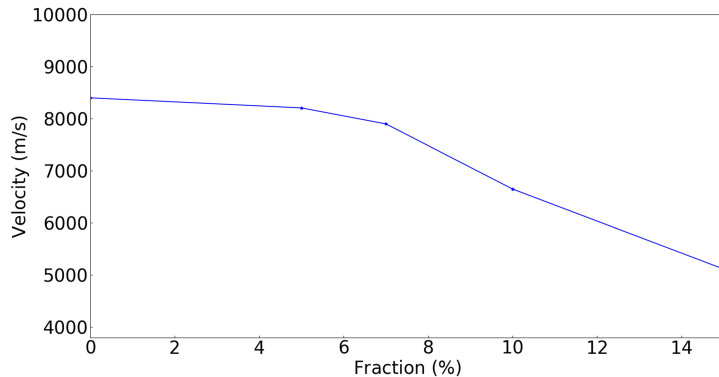


**Figure 11.** The magnitude of detonation velocity for the detonation of aluminized HMX explosive with different Al mass fractions: 5%, 7%, 10%, and 15%.

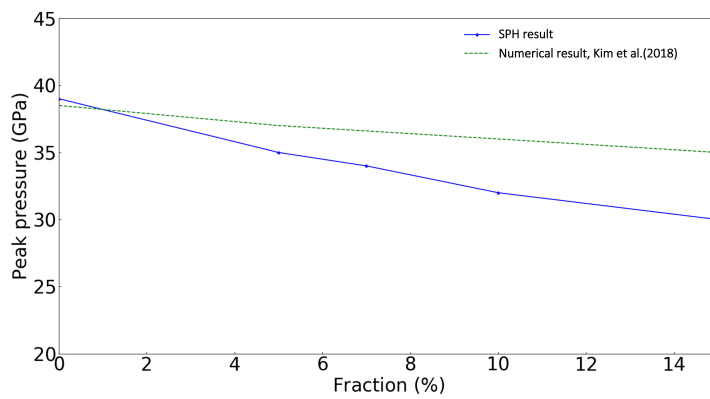


**Figure 12.** Comparison of the peak pressure magnitudes obtained from the numerical results [9] and SPH for the detonation of aluminized HMX explosive with different Al mass fractions: 5%, 7%, 10%, and 15%.

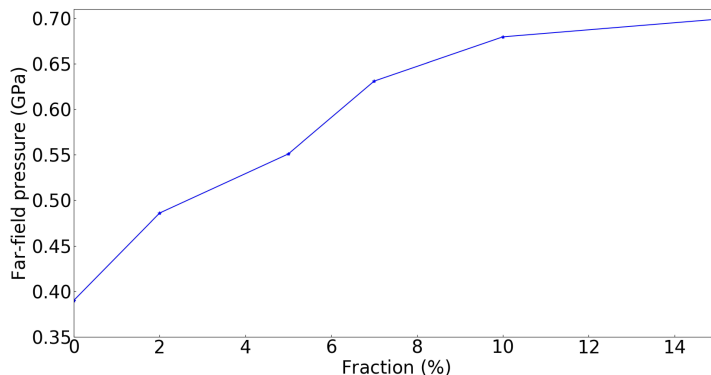


**Figure 13.** The magnitude of far-field pressure for the detonation of aluminized HMX explosive with different Al mass fractions: 2%, 5%, 7%, 10%, and 15% at 0.18 ms.

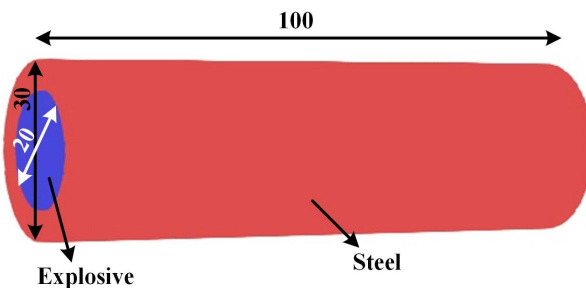


**Figure 14.** The initial geometry of the cylindrical steel confiner (all dimensions for length are in mm).

ratio. However, due to the released energy generated by the combustion of Al particles, the magnitude of pressure in the far-field increases with the rise of Al mass fraction.

- The interaction between the steel confiner and the detonation of aluminized explosive has been investigated by using SPH for the first time, and the expansion of the steel confiner can be predicted by density-adaptive SPH very well.

Concerning future work, more cases related to the brisance performance of the aluminized explosive detonation with different mass fractions of Al particles will be conducted. Furthermore, the prediction of the detonation of non-ideal explosives using different EOSs, namely JWL, JWL++, and I & G models, will be investigated and compared in terms of the shock wave propagation and brisance performance.

### Acknowledgements

The authors gratefully acknowledge the efforts and suggestions of the reviewers to improve the manuscript. This research was supported by the Natural Science Foundation of Jiangsu province of China (No. BK20210319) and the National Natural Science Foundation of China (No. 12002171).

### Data Availability Statement

The data that support the findings of this study are available from the corresponding author, Guangyu Wang, upon reasonable request.

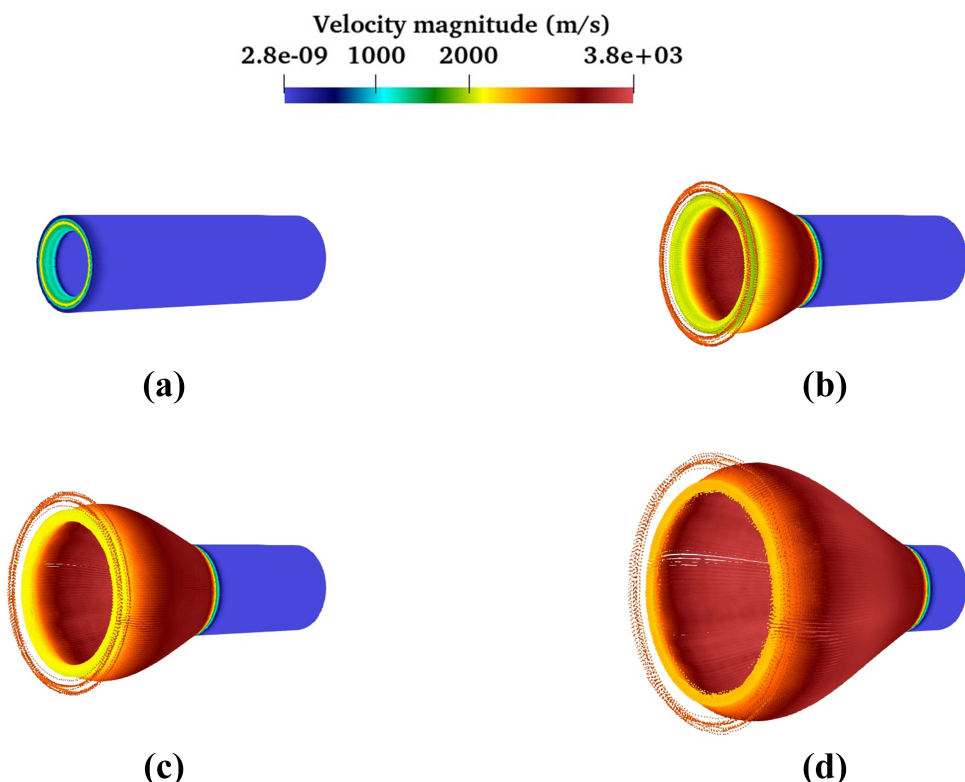


**Figure 15.** The temporal evolution of the expansion of the steel confiner generated by the explosive detonation at a time of (a) 4  $\mu$ s, (b) 6  $\mu$ s, (c) 8  $\mu$ s, and (d) 12  $\mu$ s.

## References

- [1] M. A. Cook, A. S. Filler, R. T. Keyes, W. S. Partridge, W. Ursenbach, Aluminized explosives, *J. Phys. Chem.* **1957**, *61*, 189–196.
- [2] V. W. Manner, S. J. Pemberton, J. A. Gunderson, T. J. Herrera, J. M. Lloyd, P. J. Salazar, P. Rae, B. C. Tappan, The role of aluminum in the detonation and post-detonation expansion of selected cast HMX-based explosives, *Propellants Explos. Pyrotech.* **2012**, *37*, 198–206.
- [3] D. Y. Liu, L. Chen, C. Wang, J. Y. Wu, Aluminum acceleration and reaction characteristics for aluminized CL-20-based mixed explosives, *Propellants Explos. Pyrotech.* **2018**, *43*, 543–551.
- [4] D. Y. Liu, P. Zhao, S. H. Chan, H. H. Hng, L. Chen, Effects of nano-sized aluminum on detonation characteristics and metal acceleration for RDX-based aluminized explosive, *Def. Technol.* **2021**, *17*, 327–337.
- [5] P. C. Souers, S. Anderson, J. Mercer, E. McGuire, P. Vitello, JWL + +: a simple reactive flow code package for detonation, *Propellants Explos. Pyrotech.* **2000**, *25*, 54–58.
- [6] C. M. Tarver, E. M. McGuire, 12 International Detonation Symposium, San Diego, CA (US), August 11 – 16 2002.
- [7] C. M. Tarver, Ignition and growth reactive flow modeling of recent HMX/TATB detonation experiments, *AIP Conf. Proc.* **2017**, *1793*, 030004.
- [8] E. K. Anderson, T. D. Aslam, S. I. Jackson, The effect of transverse shock propagation on the shock-to-detonation transition process for an insensitive explosive, *Proc. Combust. Inst.* **2015**, *35*, 2033–2040.
- [9] W. Kim, M. Gwak, Y. Lee, J. J. Yoh, A two-phase model for aluminized explosives on the ballistic and brisance performance, *J. Appl. Phys.* **2018**, *123*, 055902.
- [10] R. A. Gingold, J. J. Monaghan, Smoothed particle hydrodynamics: theory and application to non-spherical stars, *Mon. Not. R. Astron. Soc.* **1977**, *181*, 375–389.
- [11] L. B. Lucy, A numerical approach to the testing of the fission hypothesis, *Astron. J.* **1977**, *82*, 1013–1024.
- [12] M. B. Liu, G. R. Liu, Z. Zong, K. Y. Lam, Computer simulation of high explosive explosion using smoothed particle hydrodynamics methodology, *Comput. Fluids* **2003**, *32*, 305–322.
- [13] G. Yang, Y. K. Fu, D. Hu, X. Han, Feasibility analysis of SPH method in the simulation of condensed explosives detonation with ignition and growth model, *Comput. Fluids* **2013**, *88*, 51–59.
- [14] G. Y. Wang, G. R. Liu, Q. Peng, S. De, D. L. Feng, M. B. Liu, A 3D smoothed particle hydrodynamics method with reactive flow model for the simulation of ANFO, *Propellants Explos. Pyrotech.* **2015**, *40*, 566–575.
- [15] G. Y. Wang, G. R. Liu, Q. Peng, S. De, A SPH implementation with ignition and growth and afterburning models for aluminized explosives, *Int. J. Comput. Methods* **2017**, *14*, 1750046.
- [16] E. L. Lee, C. M. Tarver, Phenomenological model of shock initiation in heterogeneous explosives, *Phys. Fluids* **1980**, *23*, 2362–2372.
- [17] W. Dehnen, H. Aly, Improving convergence in smoothed particle hydrodynamics simulations without pairing instability, *Mon. Not. R. Astron. Soc.* **2012**, *425*, 1068–1082.
- [18] G. R. Liu, M. B. Liu, Smoothed particle hydrodynamics: a mesh-free particle method, World Scientific, 2003.
- [19] J. J. Monaghan, Simulating free surface flows with SPH, *J. Comput. Phys.* **1994**, *110*, 399–406.
- [20] J. J. Monaghan, Smoothed particle hydrodynamics, *Rep. Prog. Phys.* **2005**, *68*, 1703–1759.
- [21] M. B. Liu, Z. L. Zhang, D. L. Feng, A density-adaptive SPH method with kernel gradient correction for modeling explosive welding, *Comput. Mech.* **2017**, *60*, 513–529.
- [22] C. Peng, S. Wang, W. Wu, H. S. Yu, C. Wang, J. Y. Chen, LO-QUAT: an open-source GPU-accelerated SPH solver for geotechnical modeling, *Acta Geotech.* **2019**, *14*, 1269–1287.
- [23] M. Hu, G. Y. Wang, G. R. Liu, Q. Peng, The application of Godunov SPH in the simulation of energetic materials, *Int. J. Comput. Methods* **2020**, *17*, 1950028.
- [24] V. M. Boiko, S. V. Poplavski, Self-ignition and ignition of aluminum powders in shock waves, *Shock Waves* **2002**, *11*, 289–295.
- [25] A. L. Kuhl, J. B. Bell, V. E. Beckner, Heterogeneous continuum model of aluminum particle combustion in explosions, *Combust. Explos. Shock Waves* **2010**, *46*, 433–448.
- [26] F. Togashi, J. D. Baum, E. Mestreau, R. Löhner, D. Sunshine, Numerical simulation of long-duration blast wave evolution in confined facilities, *Shock Waves* **2010**, *20*, 409–424.
- [27] J. Y. Chen, D. L. Feng, S. X. Deng, C. Peng, F. S. Lien, GPU-accelerated smoothed particle hydrodynamics modeling of jet formation and penetration capability of shaped charges, *J. Fluids Struct.* **2020**, *99*, 103171.
- [28] P. W. Randles, L. D. Libersky, Smoothed particle hydrodynamics: some recent improvements and applications, *Comput. Methods Appl. Mech. Eng.* **1996**, *139*(1-4), 375–408.
- [29] C. M. Tarver, J. Forbes, F. Garcia, P. A. Urtiew, Manganin gauge and reactive flow modeling study of the shock initiation of PBX 9501 620 (1) (2002) 1043–1046.
- [30] S. I. Jackson, M. Short, Scaling of detonation velocity in cylinder and slab geometries for ideal, insensitive and non-ideal explosives, *J. Fluid Mech.* **2015**, *773*, 224–266.
- [31] D. L. Feng, M. B. Liu, H. Q. Li, G. R. Liu, Smoothed particle hydrodynamics modeling of linear shaped charge with jet formation and penetration effects, *Comput. Fluids* **2013**, *86*, 77–85.
- [32] S. Hiermaier, D. Konke, A. J. Stilp, K. Thoma, Computational simulation of the hypervelocity impact of Al-spheres on thin plates of different materials, *Int. J. Impact Eng.* **1997**, *20*, 363–374.

Manuscript received: July 24, 2021  
Version of record online: November 12, 2021